

The Governing Dynamics of the Secondary Eyewall Formation of Typhoon Sinlaku (2008)

Y. QIANG SUN

*Department of Atmospheric and Oceanic Sciences, Peking University, Beijing, China, and Department of Meteorology,
The Pennsylvania State University, University Park, Pennsylvania*

YUXIN JIANG AND BENKUI TAN

Department of Atmospheric and Oceanic Sciences, Peking University, Beijing, China

FUQING ZHANG

Department of Meteorology, The Pennsylvania State University, University Park, Pennsylvania

(Manuscript received 7 February 2013, in final form 21 July 2013)

ABSTRACT

Through successful convection-permitting simulations of Typhoon Sinlaku (2008) using a high-resolution nonhydrostatic model, this study examines the role of peripheral convection in the storm's secondary eyewall formation (SEF) and its eyewall replacement cycle (ERC). The study demonstrates that before SEF the simulated storm intensifies via an expansion of the tangential winds and an increase in the boundary layer inflow, which are accompanied by peripheral convective cells outside the primary eyewall. These convective cells, which initially formed in the outer rainbands under favorable environmental conditions and move in an inward spiral, play a crucial role in the formation of the secondary eyewall. It is hypothesized that SEF and ERC ultimately arise from the convective heating released from the inward-moving rainbands, the balanced response in the transverse circulation, and the unbalanced dynamics in the atmospheric boundary layer, along with the positive feedback between these processes.

1. Introduction

The secondary eyewall formation (SEF) and the eyewall replacement cycle (ERC) occur frequently in intense tropical cyclones (TCs) (Willoughby et al. 1982; Hawkins et al. 2006; Houze et al. 2007; Kuo et al. 2009; Sitkowski et al. 2011). They are often associated with rapid changes in a TC's intensity and structures characterized by an abrupt increase in a TC's minimum pressure and the expansion of the gale-force wind radii. During SEF and ERC, the secondary eyewall becomes established whereas the primary eyewall weakens or decays. The completion of ERC is usually followed by a re-intensification process of the TC.

The mechanisms that lead to SEF and ERC have constituted an active area of research over the past few

decades. And, based on these studies, it is now widely accepted that both favorable external environmental conditions and internal dynamics play essential roles in SEF and ERC. Environmental conditions such as the sea surface temperature, moisture distribution, and vertical wind shear are closely related to a TC's maximum intensity (e.g., Emanuel et al. 2004; Wang and Wu 2004). Additionally, environmental conditions may also influence the TC structure, which has been suggested in a number of studies (e.g., Wang 2009; Hill and Lackmann 2009). Further, some theoretical and modeling studies have indicated that vortex Rossby waves (VRW) are critical to SEF (e.g., Montgomery and Kallenbach 1997; Chen and Yau 2001; Wang 2002a,b; Martinez et al. 2011; Menelaou et al. 2012). The key point of vortex Rossby wave theory is that the vortex Rossby waves emitted from the primary eyewall and propagated along the radial direction can accelerate the mean tangential winds at a distance from the storm center through eddy momentum flux convergence. The accumulation of the eddy momentum could generate the secondary wind maximum

Corresponding author address: Prof. Benkui Tan, Department of Atmospheric and Oceanic Sciences, Peking University, Yiheyuan Road 5, Zhongguancun, Haidian, Beijing 100871, China.
E-mail: bktan@pku.edu.cn

necessary for SEF. The role of VRWs in secondary eyewall formation has been shown by idealized numerical experiments (e.g., Qiu et al. 2010) and by high-resolution numerical simulations of observed storms (e.g., Abarca and Corbosiero 2011). These studies emphasized the role of the VRWs; however, Moon et al. (2010) questioned whether these overly simplified and highly idealized assumptions are truly applicable to real-world TCs. Moreover, Judt and Chen (2010), also on the basis of high-resolution simulations, demonstrated that VRWs may have contributed very little to the SEF of Hurricane Rita. Further, they concluded that a large accumulation of convectively generated potential vorticity (PV) anomalies in the rainband region constituted a key factor in the formation of that hurricane's secondary eyewall. The effect of the heat from the rainband on the intensity and structure of storms has also been examined in other studies (Wang 2009; Wu et al. 2009; Moon and Nolan 2010). Wang (2009) explored the role of spiral rainband heating in the intensity change of an idealized TC and found that heat in the outer spiral rainbands may favor the development of annular hurricane structures and concentric eyewalls. Moon and Nolan (2010) found that if the rainband heating lasts long enough, the accelerated tangential circulation could wrap around the entire vortex and remain coherent for a long time after the heat from the rainbands has dissipated.

In addition to the above ideas, some other useful concepts pertaining to SEF have been developed using simple models. Kuo et al. (2004, 2008) explored the two-dimensional, nondivergent vortex dynamic interactions between two or more vorticity patches that varied in regard to size, separation, and intensity. They demonstrated that concentric vorticity features form through the axisymmetrization of weaker patches of vorticity around a strong core of vorticity. However, these studies have some key limitations in terms of explaining vortex axisymmetrization in realistic hurricane-like flows. In full-physics simulations of SEF, such as in the current study, convectively generated vorticity anomalies outside the primary eyewall are comparable in terms of magnitude to the mean vorticity of the primary eyewall region, but these anomalies have a smaller horizontal scale than the characteristic diameter of the primary eyewall. Convectively generated vorticity anomalies with a large amplitude and small scale resist axisymmetrization by the large-scale hurricane vortex (Dritschel and Waugh 1992; Enagonio and Montgomery 2001). More recently, Terwey and Montgomery (2008) proposed what is known as the beta skirt axisymmetrization (BSA) formation hypothesis for the secondary eyewall formation. The main points of BSA include the existence of a region with moderate horizontal strain deformation and a low-level

radial potential vorticity gradient associated with the primary eyewall flow, moist convective available potential energy, and a wind–moisture feedback process at the air–sea interface. To allow nascent convection to mature and form the secondary eyewall, the filamentation time scale derived by Rozoff et al. (2006) should be longer than the convective lifetime (approximately 30 min).

Wu et al. (2012) and Huang et al. (2012) simulated the SEF–ERC in Sinlaku (2008) using the Advanced Research Weather Research and Forecasting model (WRF; Skamarock et al. 2008) and an ensemble data assimilation method (Meng and Zhang 2008a,b) along with three special observational parameters shown in Wu et al. (2010). They proposed a new paradigm for SEF in which an unbalanced boundary layer response to an expanding swirling wind field is emphasized. The boundary layer process begins with a broadening of the tangential winds, followed by an increase in the corresponding boundary layer inflow that leads to a persistent supergradient wind near the top of the boundary layer of SEF region. This supergradient winds forces the convergence and leads to an eruption of air from the boundary layer to support convection outside the primary eyewall and thus to promote the onset of the SEF. This boundary layer–controlled pathway was originally used to explain the spinup of the primary TC vortex (Bui et al. 2009; Smith et al. 2009), but it may also come into play for the SEF, as recently noted in observations of Hurricane Rita (2005) (Didlake and Houze 2011; Bell et al. 2012; Didlake and Houze 2013) and in a numerical simulation of the Sinlaku Typhoon (2008) (Huang et al. 2012).

Whereas Huang et al. (2012)'s SEF paradigm demonstrated the role of unbalanced dynamics in the boundary layer in SEF, Rozoff et al. (2012) showed that the balanced vortex response in transverse circulation to diabatic heating above the boundary layer could be as important if not more so for the SEF. Indeed, the boundary layer and the free atmosphere processes are closely coupled for the SEF and ERC. The boundary layer process provides the water vapor and convergence necessary for deep convection to develop in the outer rainbands and, in turn, the diabatic heat from the convection feeds back positively and thus enhances the unbalanced boundary layer processes.

The current study examines the interplay between the unbalanced and balanced responses within and above the boundary in contributing to the SEF–ERC through successful simulations of Typhoon Sinlaku (2008). In addition to testing the hypotheses of Huang et al. (2012) and Rozoff et al. (2012), this study explores the development of the outer rainbands and their impact on the boundary layer processes. The paper is organized as follows. The model setup is given in section 2. The SEF

and ERC processes are described in section 3. The mechanisms of the SEF, particularly the roles of the expanding tangential winds and the interaction between the outer rainbands and the unbalanced boundary layer processes, are explored in section 4. Section 5 presents a brief discussion focused on the organization of the outer rainbands. The main conclusions are given in section 6.

2. Model setup

The SEF–ERC in Sinlaku were simulated in this study using WRF version 3.1.1 (Skamarock et al. 2008). The simulation comprises two domains with horizontal grid spacing of 10.8 and 3.6 km and domain sizes of 174×210 and 169×169 , respectively. Two-way interactive nesting is used wherein the inner nest automatically follows the TC center. The simulation has 40 vertical levels. The WRF single-moment 6-class (WSM6) microphysics scheme (Hong et al. 2004) and the Yonsei University (YSU) planetary boundary layer (PBL) scheme (Hong et al. 2006) are used in the simulation. The Kain–Fritsch cumulus parameterization is used only in the outer domain.

The 96-h WRF integration is initialized at 0000 UTC 9 September 2008 with the National Centers for Environmental Prediction’s (NCEP) Final (FNL) analysis data as the initial and boundary conditions. A simple tropical cyclone bogus scheme provided by WRF is adopted as an aid to obtaining a more realistic vortex at the beginning of the simulation.

3. Overview of our simulation

a. Track and intensity

Typhoon Sinlaku (2008) began as a tropical disturbance on 7 September 2008 to the northeast of Manila in the Philippines. It developed into a category-2 typhoon on 9 September and reached its maximum strength as a category-4 typhoon on 10 September. Then, the storm went through ERC and began to weaken. Before reaching landfall in Taiwan, the storm evolved into a category-2 typhoon. Sinlaku happened to occur during The Observing System Research and Predictability Experiment (THORPEX) Pacific Asian Regional Campaign (T-PARC; Elsberry and Harr 2008), and its ERC and SEF processes were well captured in the research aircraft observations and satellite images (Wu et al. 2012; Huang et al. 2012).

Our simulated track, minimum sea level pressure, and maximum surface tangential wind (Fig. 1) are in overall good agreement with the best-track data from the China Meteorological Administration (CMA; <http://www.typhoon.gov.cn/>). There is a moderate track bias

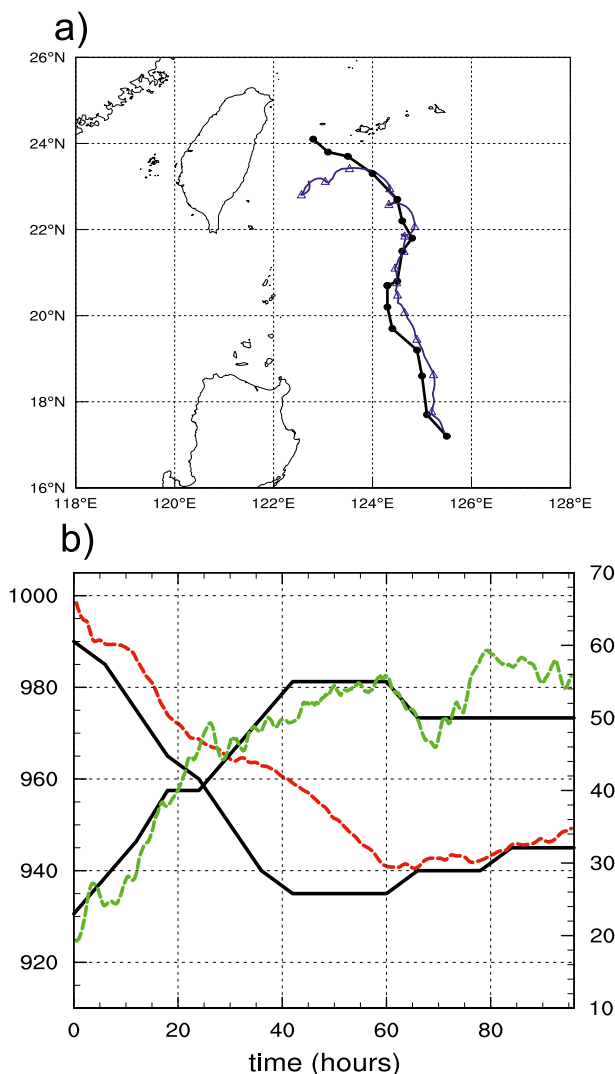


FIG. 1. The simulated (a) tracks (blue line) and (b) time evolution of the maximum tangential wind (green) and sea level pressure (red) for Typhoon Sinlaku (2008). The best-track data are shown by a black line in both panels.

after 80 h and a corresponding high bias in the maximum surface wind just before Sinlaku’s landfall when the cyclone begins to interact with Taiwan’s complex terrain. The simulated intensification of the storm is about 10 h slower than the best-track data, which is likely because of the spinup process (Fig. 1b). Nevertheless, the SEF and ERC are well simulated by the model. Figure 2 shows the time evolution of the azimuthally averaged vertical velocity and tangential winds at 1 km in the simulation, which shows that the ERC starts at around 60 h and ends at around 72 h. Note that there is no accepted definition regarding the exact beginning/ending of SEF. Here, we choose 60 h as the start time of the SEF process in our simulation mainly based on the evidence in vertical

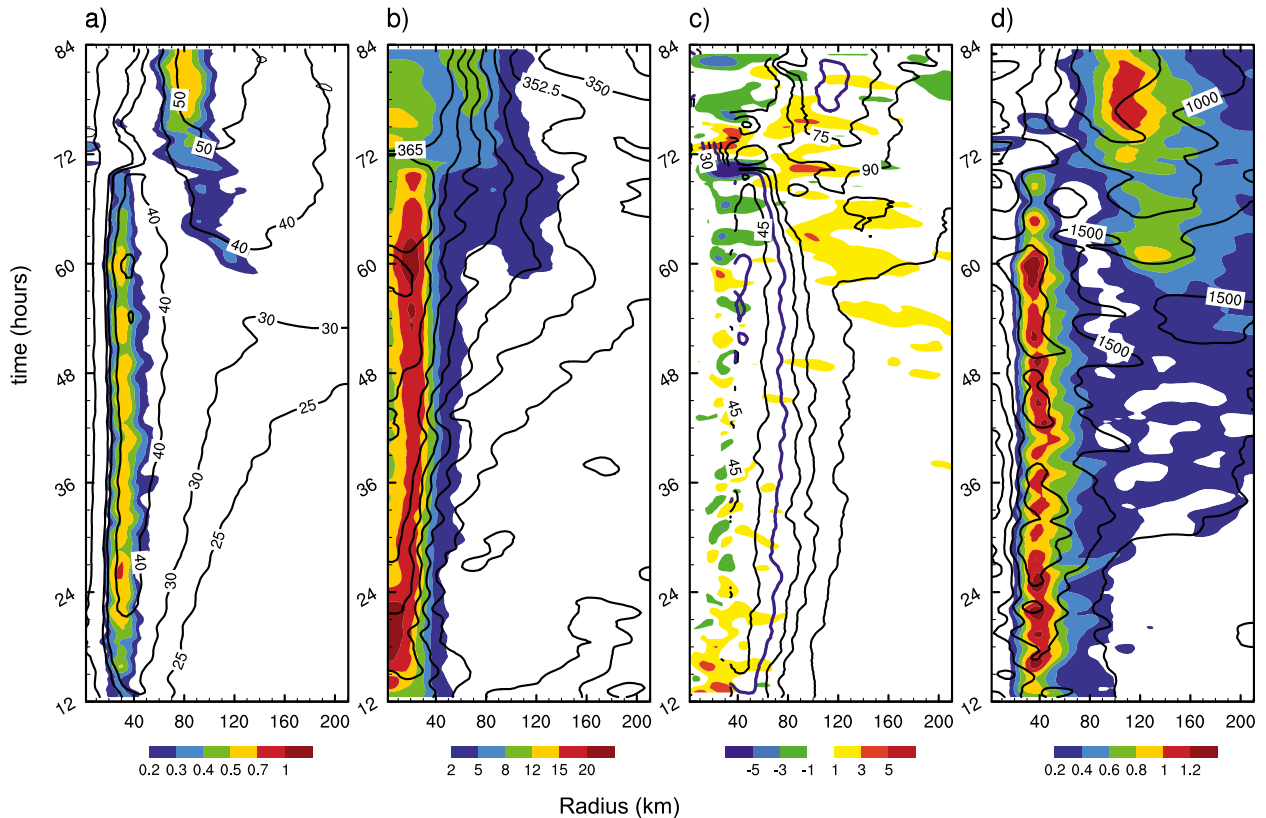


FIG. 2. Time evolution from 42 to 75 h in 3-h increments of (a) azimuthally averaged vertical velocity (m s^{-1} , shaded) and tangential wind (m s^{-1} , contours) at 1 km, (b) potential vorticity (PVU, shaded) and equivalent potential temperature (K, contours), (c) tangential wind tendency ($\text{m s}^{-1} \text{h}^{-1}$, shaded) and filamentation time scales (min, contours; blue line is 60 min), and (d) rainwater mixing ratio (g kg^{-1} , shaded) and column maximum CAPE (J kg^{-1} , contours).

velocity shown in Fig. 2a. This value could change slightly with different contour intervals, but such a change would not affect our analysis. The primary eyewall, characterized by the maximum vertical velocity and maximum tangential wind at a radius of around 40 km, begins to weaken at 60 h and to disappear at around 72 h. At the same time, the secondary eyewall, characterized by the secondary maximum vertical velocity and maximum tangential wind at around 120 km, begins to grow and is finally replaced by the primary eyewall. The ERC in our simulation is 5 h later than in Wu et al. (2012) and Huang et al. (2012), which is consistent with the slight delay of the simulated intensification process compared with the best-track data.

It is also worth noting that the simulated storm undergoes an intensification process from 40 to 60 h before SEF, which is common for ERCs that occur in intense storms (Houze et al. 2007). This intensification process is also associated with an expansion of the tangential winds and the enhancement of the inflow and outflow within and above the boundary layer, respectively, the role of which will be discussed in detail in section 4.

b. Azimuthal-mean circulation

The intensification process of a TC, particularly in regard to the ERC, is inherently three dimensional. Yet, the axisymmetric “mean field” view can provide a useful vantage point for understanding the system-scale aspects of these processes (e.g., Smith et al. 2009; Bell et al. 2012; Rozoff et al. 2012). Figure 3 shows the time evolution of the azimuthally averaged tangential winds and radial winds on the (r, z) plane. To clearly show the low-level character, the display length scale in z direction below 3-km altitude is artificially doubled. Though the location of the maximum tangential wind associated with the primary eyewall remains almost unchanged before the ERC from 40 to 60 h, there is an apparent outward and upward expansion of the tangential winds during this period. The 25 m s^{-1} contour line, for example, is only limited within 150-km radius at 42 h but shifts to a far outer region beyond 280 km and can reach or even exceed 3-km altitude at 51 h. The secondary maximum of the tangential winds is centered at 200 km at 54 h. This maximum center (lies outside the domain of

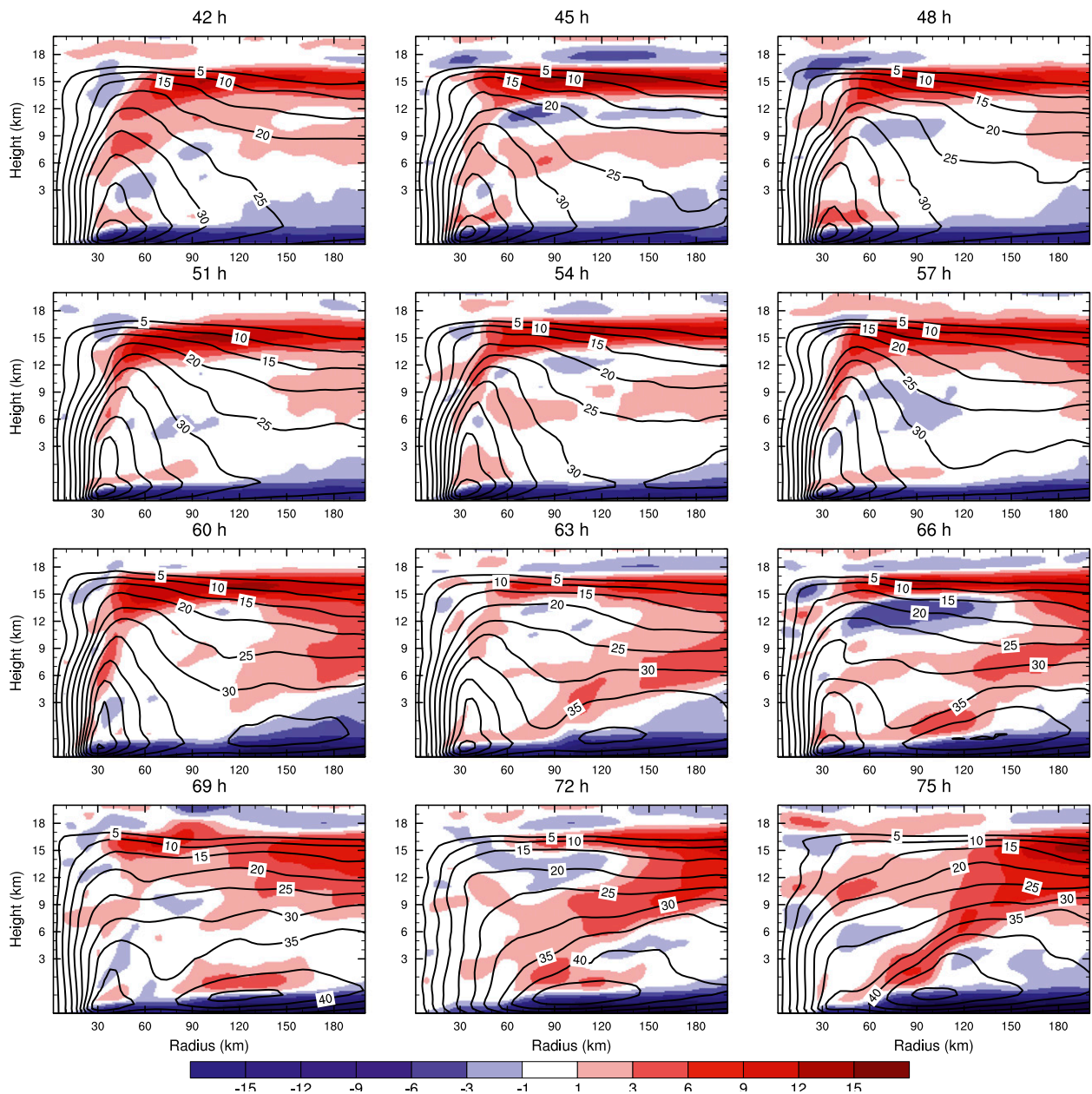


FIG. 3. Time evolution from 42 to 75 h in 3-h increments of the radius–height cross section of azimuthally averaged tangential winds (black contours from 0 to 60 m s^{-1} every 5 m s^{-1}) and radial winds (shaded, from -15 to 15 m s^{-1} every 3 m s^{-1}). The vertical resolution below 3 km is double that of above 3 km.

Fig. 3) forms at around 45 h and is closely coupled to the outer rainbands. It moves to 150 km, and then intensifies further to reach a value exceeding 35 m s^{-1} at 60 h, which, along with a strong vertical velocity, defines the beginning of the secondary eyewall. At the same time, the primary maximum tangential wind begins to weaken and finally dies out at around 72 h, and the secondary maximum tangential wind continues to move inward and to increase in strength until 75 h when it reaches its

maximum of more than 50 m s^{-1} . At this point, the ERC is complete.

The radial inflow in the boundary layer before 40 h is widely distributed from the outer region to the primary eyewall. This boundary layer inflow increases relatively slowly from 40 to 60 h but with a jump of magnitude in the outer region at 60 h. After the secondary eyewall is established, the inflow within the primary eyewall begins to weaken and almost disappears at the completion of

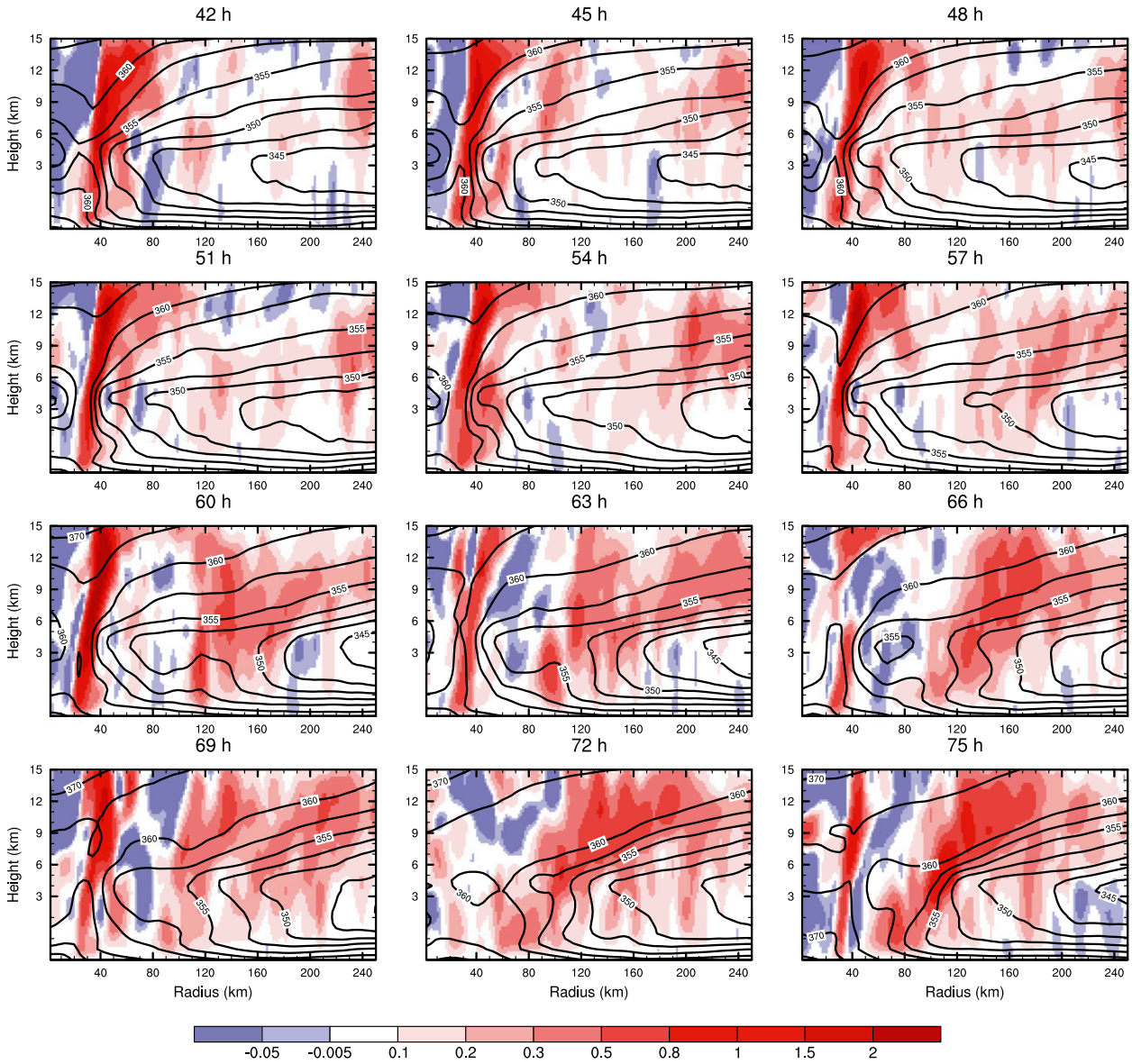


FIG. 4. Time evolution from 42 to 75 h in 3-h increments of the the radius–height cross section of azimuthal vertical velocity (m s^{-1} , shaded) and equivalent potential temperature (K, contours) from 42 to 75 h.

the ERC. At the same time, the boundary layer inflow outside the secondary eyewall increases abruptly at around 60 h and continues to grow in magnitude during the ERC process. At upper levels of the troposphere, the outflow extends from the primary eyewall to the outer region and remains almost unchanged before the ERC is complete. The outflow inside the secondary eyewall begins to weaken after the SEF is established and disappears when the ERC is complete. At the same time, the outflow in the outer region changes abruptly when the ERC starts, and a new maximum outflow is established at around 200 km after the ERC is complete,

which extends from above the boundary layer of the outer region downward into the boundary layer where the secondary eyewall is located.

A clearer picture of the SEF and ERC can be seen in the vertical velocity field (Fig. 4). Though there is always a positive vertical velocity maximum associated with primary eyewall, this maximum weakens when the ERC begins and eventually disappears when the ERC is complete. Outside the primary eyewall, some vertical velocity perturbations persistently form in the mid- to upper troposphere. These vertical velocity perturbations are associated with peripheral convective cells in

the outer rainbands; these cells then gradually move inward and develop into strong deep convection at 60 h that persist strongly until the end of the simulation.

The simulated moist entropy structure in the primary and secondary eyewall regions (Fig. 4) assumes a similar feature as that observed in Hurricane Rita (2005) (Bell et al. 2012): “The vertical profile of the equivalent potential temperature in the primary eyewall evolved from nearly constant with height above the surface layer to a negative slope. In contrast, the secondary eyewall evolved from a negative slope toward a constant with height. This suggests a transition from a conditionally unstable profile toward moist neutrality in the secondary eyewall, and vice versa for the primary eyewall.”

4. Mechanisms of the secondary eyewall formation

The mechanisms of the SEF involves complex physical processes in which the expansion of the tangential winds and the interaction between the outer rainbands and the unbalanced boundary layer processes make important contributions to the SEF. Here, we take a closer look at these processes.

a. Dynamical features within and just above the boundary layer

As noted in the introduction, Huang et al. (2012) observed a progressive enhancement of the unbalanced boundary layer dynamics characterized by supergradient winds and positive agradient forces in the SEF region before SEF in their simulated Sinlaku. Here, we explore the boundary layer flow to determine whether these unbalanced features also exist in our simulation of the same storm. The agradient force (AF) and the agradient wind (AW) are given by

$$\text{AF} = -\frac{1}{\bar{\rho}} \frac{\partial \bar{p}}{\partial r} + f\bar{v} + \frac{\bar{v}^2}{r} \quad \text{and} \quad (1)$$

$$\text{AW} = \bar{v} - \bar{v}_g, \quad (2)$$

where \bar{v}_g is the gradient wind. The WRF AFs and AWs averaged over the primary eyewall (20–50 km), the moat (50–100 km), the secondary eyewall (100–150 km), and the outer region (150–200 km) are shown in Fig. 5. As the secondary eyewall seems to be continually evolving and contracting through much of the process, the choice of a fixed radial range as the averaging domain has its limitation. However, the results we show here still hold with slight alteration of the domain (e.g., change the moat region to be 80–110 km). As can be seen from Fig. 5, below 1.5 km the primary eyewall remains in a state of strong positive AFs (AWs) until 72 h, and the maximum

magnitude of the AFs (AWs) reaches more than $21 \text{ m s}^{-1} \text{ h}^{-1}$ (7 m s^{-1}). Then, both the AFs and AWs weaken. In the moat region, the boundary layer flow above the surface layer assumes a state of weak positive AFs before 65 h at a magnitude of $3\text{--}6 \text{ m s}^{-1} \text{ h}^{-1}$, which is a sign of expanding tangential winds associated with the intensification of the storm. After 65 h, the moat is in a state of moderately positive AF and then turns into a state of strong AF from 70 h on, thereby reflecting the contraction and intensification of the secondary eyewall. In the SEF region above 800 m, as in Huang et al. (2012), the boundary layer flow assumes weak positive AF and AW until 55 h. Then the AF and AW grow progressively stronger and larger. At 60 h, the AF and AW grow abruptly as a sign of the onset of the SEF. From 60 h on, the secondary eyewall region remains in a state of strong AF and strong AW for the ERC, which extends even beyond the boundary layer up to as high as around 5 km. In the outer region above 800 m, the flow is in a state of quasi-gradient balance, in which the AF and AW are weak. From 51 h on, the AF and AW of the flow each increase slightly just prior to the SEF.

b. The role of the expanding wind field in SEF

The previous section shows that before the SEF the tangential winds expand continuously outward from the primary eyewall. This expanding wind field may facilitate the SEF. The enhanced local surface wind increases the surface entropy fluxes and thus favors enhanced convection (Xu and Wang 2010a,b). According to Rozoff et al. (2012), the expanding wind field enhances the inertial stability, which, in turn, improves kinetic energy efficiency (KEE) such that more latent heat associated with convection is retained in the TC as kinetic energy with an expanding wind field.

To test Rozoff et al.’s (2012) hypothesis, the Sawyer–Eliassen (S–E) model (see appendix) is adopted in this study. It should be pointed out here that for the S–E equation to be strictly valid, the flow must satisfy both the hydrostatic and the gradient wind balance. In the boundary layer, the eyewall, and other regions with abrupt changes or strong gradients, the two balances may break down locally (Fig. 5). Nevertheless, the S–E equation is a useful tool that has been used widely in the study of the intensity change of TCs (e.g., Bui et al. 2009; Fang and Zhang 2011). The S–E model used here is the same as in Fang and Zhang (2011), which is to a large extent consistent (and shares similar limitations) with the linear model used in Rozoff et al. (2012).

Figure 6 shows the azimuthally mean vertical and radial velocities from WRF and from the S–E-balanced model at 42, 51, and 60 h, respectively. It is evident that the vertical velocities associated with both the primary

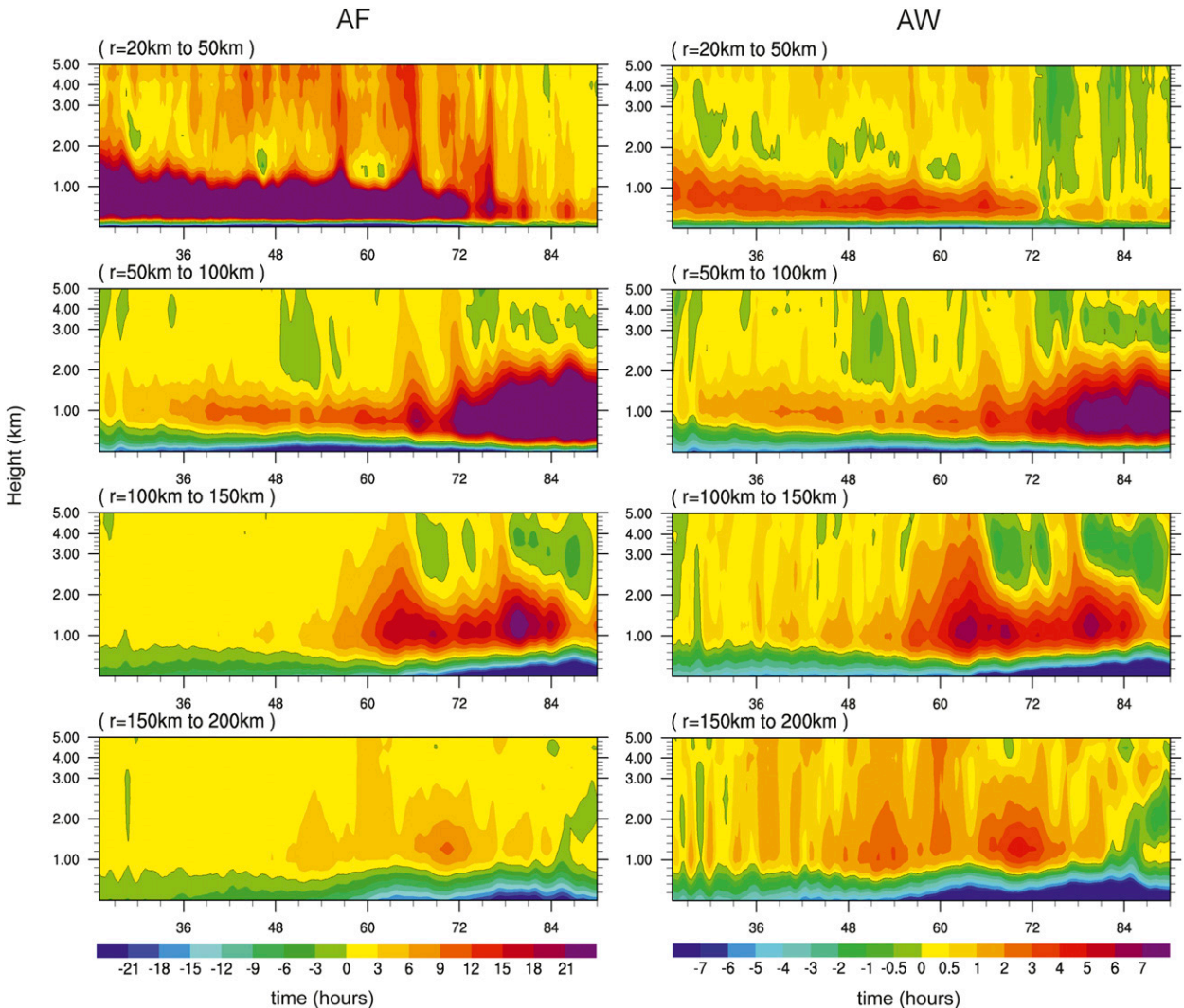


FIG. 5. The time–height section of azimuthally averaged (left) AF ($\text{ms}^{-1}\text{h}^{-1}$) and (right) AW (ms^{-1}) over (top to bottom) the primary eyewall (20–50 km), the moat (50–100 km), the secondary eyewall (100–150 km), and the outer region (150–200 km). Vertical resolution as in Fig. 3.

and secondary eyewalls and the inflow in the boundary layer in WRF are well captured by the S–E model, though the derived balanced vertical velocity is slightly smaller in the inner primary eyewall, similar to Rozoff et al. (2012)’s findings based on an idealized case study. Notable differences in the upper outflow can be found: specifically, the magnitudes of the outflow are generally larger in WRF than in the S–E model, although this is not the case at 42 h. This result is consistent with Fudeyasu and Wang (2011), who attribute it to the strong agradient wind. It is also interesting to note that the outflow just above the boundary layer is not well captured in the S–E model, which is also associated with the agradient wind there (Fig. 5). The linear S–E model calculation of the relative contributions of each term, including the azimuthally

diabatic heating, the subgrid-scale friction, and the eddy forcing was also conducted (diabatic heating dominates the results; not shown).

To further elucidate the role of the expanding wind field, sensitivity experiments similar to those reported in Rozoff et al. (2012) are also conducted with the S–E model. Experiments C1 and C2 are the control experiments at 42 and 60 h in which the background vortex structure and the forcing are derived from the WRF simulations at the same output times. Experiment E1 uses the vortex structure at 60 h but uses the forcing derived at 42 h, whereas experiment E2 uses the vortex structure at 42 h but the forcing at 60 h. As in Rozoff et al. (2012), the inertial stability decreases in the primary eyewall and in the inner-core region while it increases outside the primary eyewall especially in the

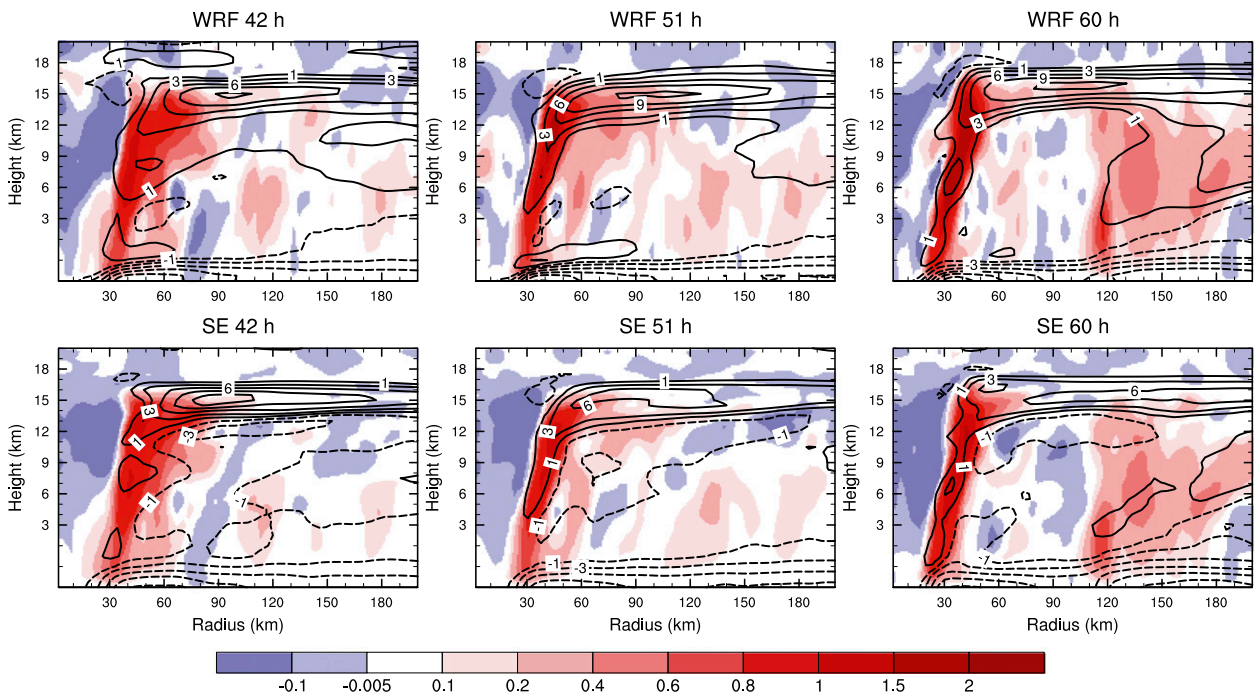


FIG. 6. Comparison between (top) WRF simulation and (bottom) S-E model results at (left to right) 42, 51, and 60 h. Shaded is the vertical velocity (m s^{-1}). Contours are the radial velocities (negative values dashed; the contour values are $-15, -12, -9, -6, -3, -1, 1, 3, 6, 9, 12, \text{ and } 15 \text{ m s}^{-1}$).

SEF region (Fig. 7). An expanded heating profile from 42 to 60 h is also given (Fig. 7).

Figure 8 shows the diagnosed tangential wind tendency in the sensitive experiments and their differences. The tangential wind tendency is calculated according to this formula:

$$\frac{\partial \bar{v}}{\partial t} + \bar{u}(f_0 + \bar{\zeta}) + \bar{w} \frac{\partial \bar{v}}{\partial z} = \bar{F}_\lambda, \quad (3)$$

where \bar{u} , $\bar{\zeta}$, \bar{w} , and \bar{F}_λ are the azimuthally averaged radial inflow, relative vorticity, vertical velocity, and radial friction force, respectively. The eddy contribution is ignored here, but we will discuss it in section 5. The result of experiment E2 is also consistent with Rozoff et al. (2012). With a smaller inertial stability at 42 h in the SEF region, the tangential wind tendency decreases and even becomes negative (the region between 70 and 120 km below 3 km). The result of experiment E1 is similar. The difference between experiment E2 and experiment C1 is also calculated.

The increased inertial stability could create a critical zone in which the SEF can take place. This hypothesis thus gives us a better understanding of the location of SEF. At 42 h the outer-core inertial stability is small; thus, the intensification principally takes place near the primary eyewall. As a result, this intensification process

only leads to the expansion of the vortex. At 60 h, the local inertial stability of the outer core is large enough to support enhanced kinetic energy efficiency, which eventually leads to the SEF.

c. Secondary local wind maximum and its relation to the outer spiral rainbands

In addition to the expansion of the tangential winds associated with the primary eyewall, a local wind maximum moves inward in the outer region. Figure 9a shows a clear picture of the evolution of the tangential winds averaged vertically from 0.5 to 3 km and radially over 20 km. As can be seen, the local wind maximum forms at around 45 h, is centered at 210 km, and becomes stronger and stronger as it moves inward. On reaching the SEF region, the local wind maximum increases rapidly in terms of strength and finally forms the secondary eyewall. There are basically two physical processes: the conservation of angular momentum and the heating from the outer rainbands, both of which enhance the local wind maximum (e.g., Smith et al. 2009; Moon and Nolan 2010). The local wind maximum is actually closely coupled to the outer rainbands and possibly driven partially by the diabatic heating from the outer rainbands (Fig. 9b). To make this point clear, we further examined the contributions of the diabatic heating from the primary

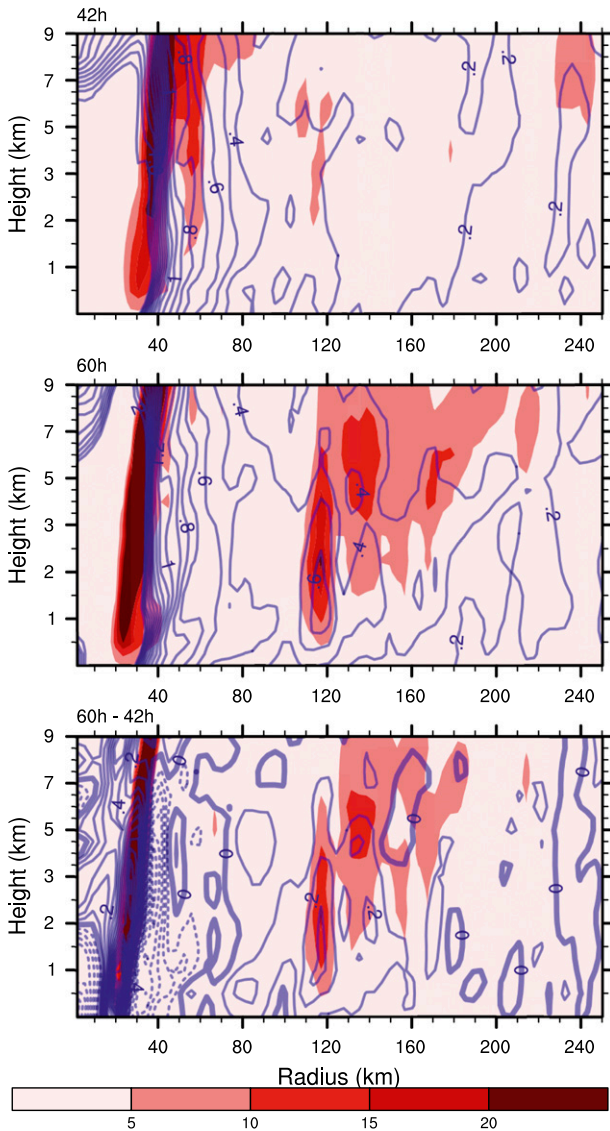


FIG. 7. Inertial stability (10^{-3} s^{-1} , contours) and diabatic heating (K h^{-1} , shaded) at (top to bottom) 42 (experiment C1) and 60 h (experiment C2), and their difference (negative values dashed).

eyewall versus that from the outer rainbands to driving the local wind maximum. First, the azimuthal-mean radial flow \bar{u} and the vertical velocity \bar{w} , forced by the azimuthally mean heating from the primary eyewall (0–80 km) and the outer rainbands (80–350 km), are calculated respectively using the S–E equation. Then, the obtained transverse circulation (\bar{u} and \bar{w}) is used to calculate the acceleration of the local maximum of the tangential winds outside the primary eyewall from Eq. (3). The result derived using S–E equation has a larger magnitude than in the simulation (Fig. 10). This can be due to several reasons. First, only diabatic heating is considered as the force here, while the friction and the subscale process might have

a negative effect. Second, the region we focus on here is the local maximum of the tangential winds, where the agradient wind is strong (Fig. 9). Thus, the assumption of S–E equation is not robust. Nevertheless, Fig. 10 shows that the dominance of the primary eyewall heating (0–80 km) is superseded by the outer rainband heating (80–350 km) from 45 h on. If we fix the vortex at 42 h, the response is much smaller, which is consistent with Fig. 8.

It is also clear from Fig. 9b that the local wind maximum is always in a state of weak supergradient winds before the SEF, which means that the flow is also in a state of weak positive gradient force in the radial direction before the SEF. The positive gradient force will force convergence (not shown), which, in turn, enhances upward motion near the top of the boundary layer, and then may act to help initiate or sustain convection aloft, as suggested by Huang et al. (2012). Thus, we conclude that under favorable conditions provided by the expanding winds, the positive feedback between the diabatic heating from the outer rainbands and the unbalanced boundary layer process could lead to the SEF and ERC.

5. Organization of the outer rainbands

Given the importance of heating from the outer rainbands, as discussed in section 4, we now explore how the outer region convection is organized into spiral rainbands with increasing intensity that subsequently lead to SEF and ERC. The role of the VRWs in the process whereby the outer rainbands become organized into the SEF is also tested.

a. Three-stage inward-moving process

We further divide the SEF process into three stages: 1) the development of peripheral convection and of the midlevel PV anomalies, 2) the axisymmetrization and organization of outer convection, and 3) the burst and maintenance of deep convection and the triggering of the SEF (Fig. 11). Stage 2 begins at around 45 h, whereas stage 3 clearly begins at around 55 h (Fig. 11). It is important to note that the three stages may be intrinsically inseparable and likewise that the key dynamic and thermodynamic processes “between” the different stages may not be exactly sequential.

1) DEVELOPMENT OF PERIPHERAL CONVECTION AND MIDDLE-LEVEL PV

Peripheral convection (outer rainbands) in tropical cyclones is common and usually composed of a number of isolated convective cells, which are generally sporadic and loosely organized in a banded structure. In our simulation, because of a favorable environment (such as high SST, large CAPE, etc.), some convective cells are

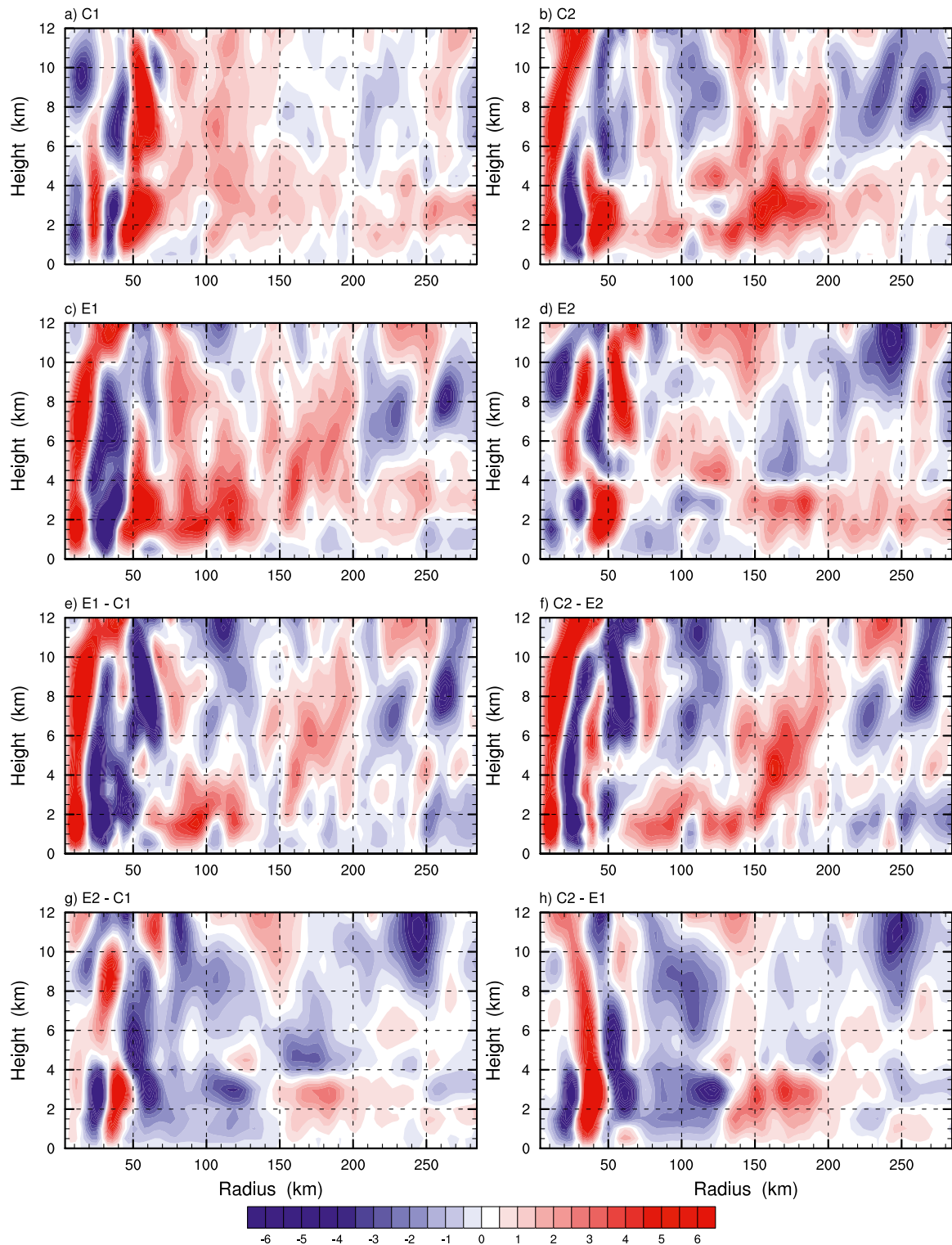


FIG. 8. Tangential wind tendency diagnosed in experiments (a) C1, (b) C2, (c) E1, and (d) E2. Experiments C1 and C2 are the control experiments at 42 and 60 h in which the background vortex structure and the forcing are derived from the WRF simulations at the same output times. Experiment E1 uses the vortex structure at 60 h but uses the forcing derived at 42 h while experiment E2 uses the vortex structure at 42 h but the forcing at 60 h. (e),(f) Differences between experiments E1 and C1 and between C2 and E2, respectively; these indicate the impact of expanding inertial stability. (g),(h) Differences between experiments E2 and C1 and between C2 and E1, respectively; these indicate the impact of expanding heat forcing.

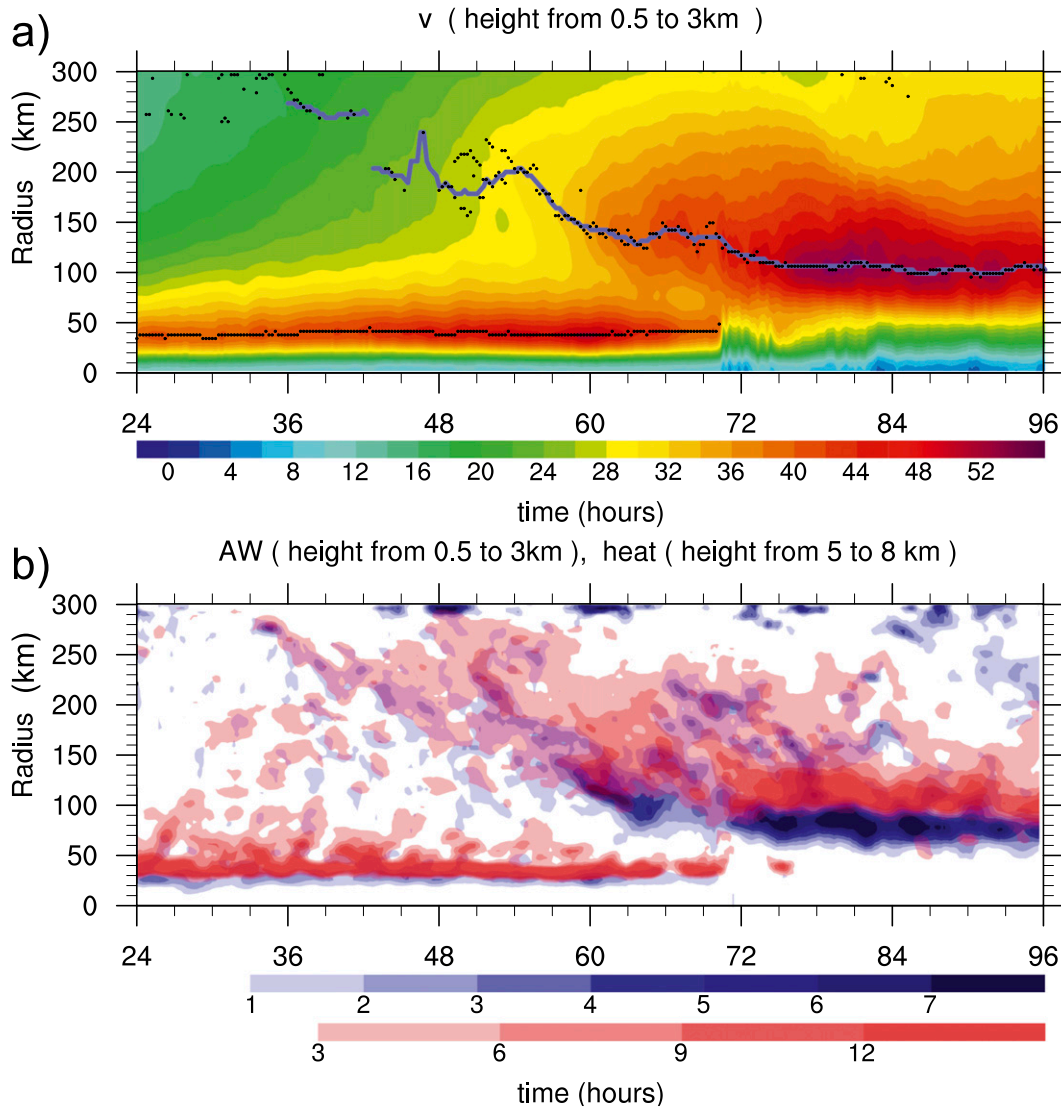


FIG. 9. (a) Time evolution of tangential wind (m s^{-1}) averaged azimuthally, vertically (0.5–3 km), and radially (20 km). The black dots indicate the locations of local maxima of the tangential wind. The thick blue line (location of secondary tangential wind maximum) was used in the calculation for Fig. 10. (b) As in (a), but for a gradient wind (m s^{-1} , blue) and diabatic heating (K h^{-1} , red, averaged vertically from 5 to 8 km).

first seen at around 20 h (not shown) in the region between 200 and 300 km east of the storm center shortly after the storm begins to intensify. Figure 12 shows the evolution of the simulated low-level radar reflectivity from 30 to 75 h that highlights the activities of the peripheral convection. From 30 to 36 h, the convective cells mainly lie to the east-northeast of the storm center, resulting from a weak westerly vertical wind shear. These convective cells are generally weaker than what are often referred to as vortical hot towers (VHTs; Montgomery et al. 2006). Nevertheless, close inspection of the convective cells indicates that they are characterized by deep moist convection and that they can reach or even exceed

12 km. Most of them have a maximum positive vorticity at a midlevel that can be more generally categorized as convectively induced vorticity anomalies [CVAs, as defined in Fang and Zhang (2010, 2011)]. After 36 h, the convective cells are no longer located solely to the east of the storm center. Instead, they begin to move in the azimuthal direction with a slight inward-moving tendency.

Consistent with the peripheral convection, the plan view of PV gives a similar evolution process (Fig. 13). The locations of PV maxima collocate well with the maximum radar reflectivity, which indicates that PV maxima are mainly caused by the heating of the convective cells (CVAs). Distinct midlevel PV maxima appear in the

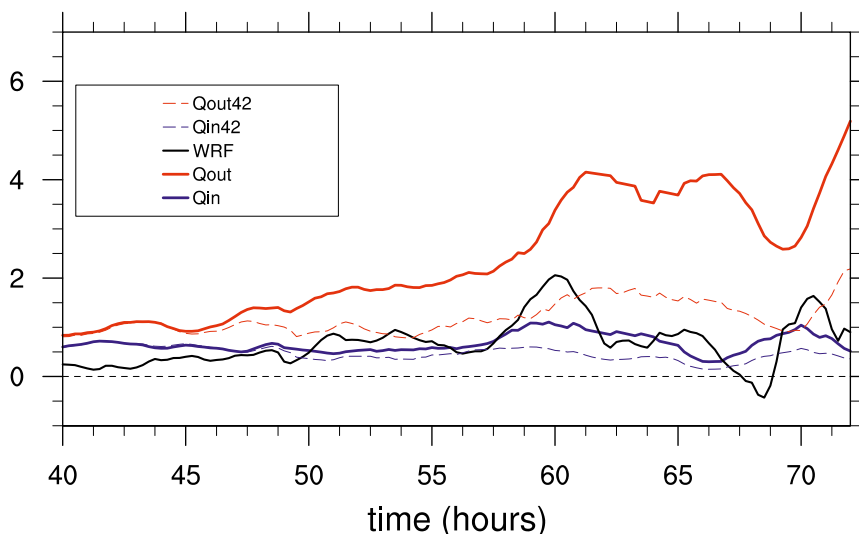


FIG. 10. Average (azimuthally, 0.5–3 km in height, 10 km in radial, 3 h in time) tangential wind tendency. Black line is the simulated tangential wind tendency, red line is S–E diagnosed tangential wind response to outer rainbands heating (80–350 km), blue line is S–E diagnosed tangential wind response to primary eyewall heating (0–80 km), and dashed lines represent the same conditions as the solid lines except that the vortex is fixed at 42 h during the calculation.

SEF region (100–150-km radii) at around 40 h (Figs. 11 and 13). Because of these midlevel PV maxima (CVAs), the azimuthal-mean PV profile is relatively flat in the SEF region, which does not favor the outward propagation of VRWs. We will discuss this in section 5b. Thus, the active convective cells are mainly due to a large CAPE (beyond 2000 J kg^{-1} ; Fig. 2d). In other words, the favorable environment contributes to the peripheral convection at this stage. Moreover, the filamentation time scale as defined by Rozoff et al. (2006) remains long enough to sustain the convection (Fig. 2c), which helps maintain the peripheral convection.

2) AXISYMMETRIZATION AND ORGANIZATION OF THE OUTER CONVECTION

After the storm reaches some certain intensity at 45 h (below 960 hPa, around 50 m s^{-1}), the axisymmetrization process of the outer rainbands becomes distinct. Though the east-northeast direction still shows the strongest convection, the peripheral convective cells begin to develop in the azimuthal direction. At around 50 h, a group of convective cells emerges to the southwest of the TC center (Figs. 12 and 13). Thus, a quasi-circular convective ring or rainband is formed, which subsequently contracts inward and intensifies (Fig. 12). Although the movement and organization of the outer rainbands are not yet fully understood, the following analysis does shed some light on this process.

During the axisymmetrization process, the peripheral precipitation increases gradually. At 50 h, a secondary maximum of the precipitation is found at the region between the radii of 150 and 200 km (Fig. 2d). The strong moist convection also acts to change the thermodynamic structure of the outer-core region. As the enhancement of low-level equivalent potential temperature is inhibited by the evaporative cooling and downdrafts in the SEF region (Fig. 4), its radial gradient increases. As in Fang and Zhang (2012), this increased thermal gradient may have contributed to the lifting of the low-level air, which would further increase the gradient of the equivalent potential temperature on the inner side through the release of latent heating and the precipitation process. This is also consistent with the S–E solution whereby a radial gradient of heating produces a balanced overturning circulation in a vortex (Shapiro and Willoughby 1982).

Further, it is worth noting that the latent heat release averaged in the whole outer core is always positive during this stage (Fig. 11). As a result, the hydrostatic adjustment process proposed by Wang (2009) is valid here. Diabatic heating would reduce the surface pressure underneath the column, and thus increase the local pressure gradient and the local tangential wind (Fig. 9b). From 45 to 55 h, the tangential wind of the vortex expands dramatically. Further, there is an apparent transient secondary maximum of the tangential wind at this stage (Figs. 3 and 9a).

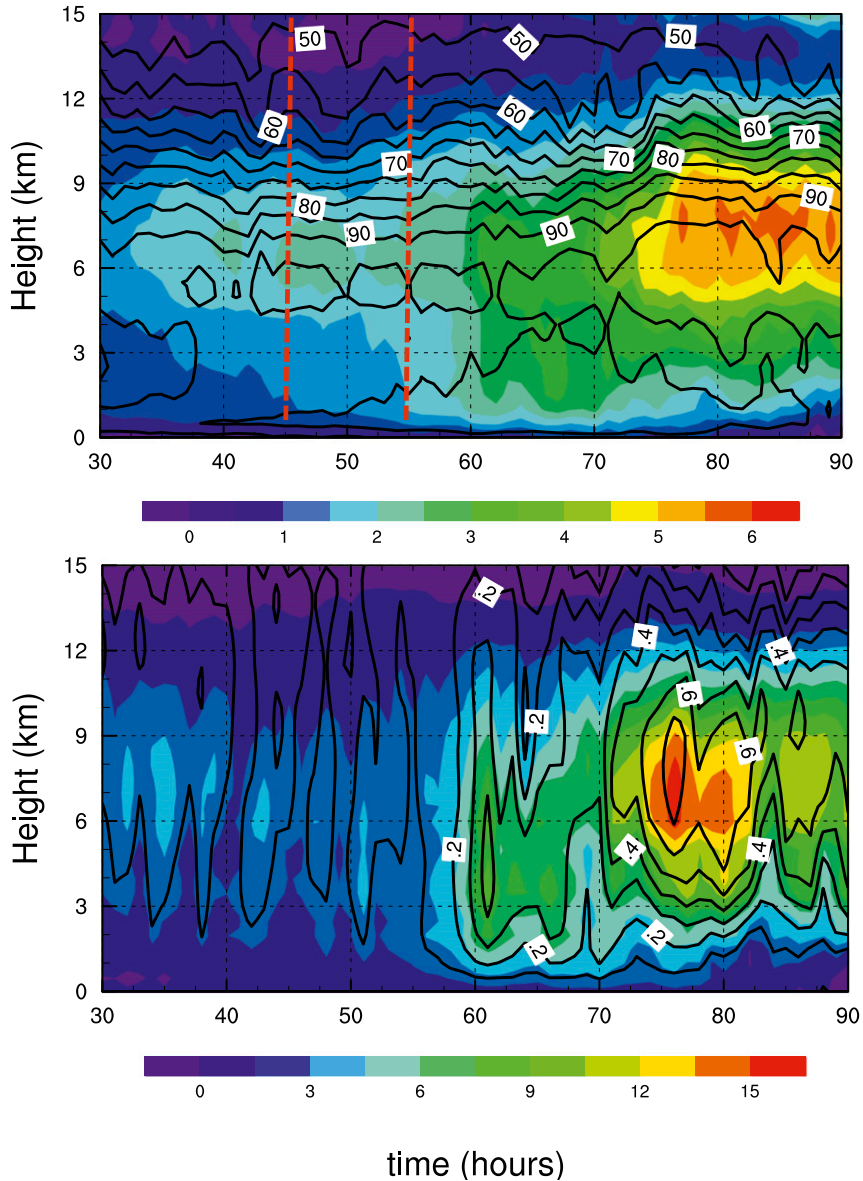


FIG. 11. Time evolution of (a) potential vorticity (PVU, shaded) and relative humidity (%), contours) and (b) latent heat (K h^{-1} , shaded) and vertical velocity (m s^{-1} , contours). Their values are averaged over the SEF region (100–150 km). The two red dashed vertical lines in (a) denote the onset of stage 2 and stage 3, respectively.

3) BURST AND MAINTENANCE OF DEEP CONVECTION AND SEF

The contraction of the outer rainbands and the expansion of the wind field in stage 2 leads to a burst of deep strong convection at around 55 h at 100–150-km radii (the future SEF region). Vigorous deep convection in this region with the release of strong latent heat further increases the inflow and thus increases the local tangential winds, and the enhanced swirling winds, in turn, increase the surface entropy fluxes (Xu and Wang 2010a,b) and so

favor efficient kinematic energy conversion (Rozoff et al. 2012) as discussed in previous sections. The increased friction associated with enhanced tangential winds then facilitates convection through unbalanced boundary dynamics. This positive feedback process not only sustains but also greatly enhances the convection in the SEF region from 55 to 60 h. The strong convection outside the primary eyewall at 60 h finally leads to the SEF.

The formation process here is also somewhat similar to that in the idealized study of Fang and Zhang (2012), except that the midlevel PV in their study is thought to

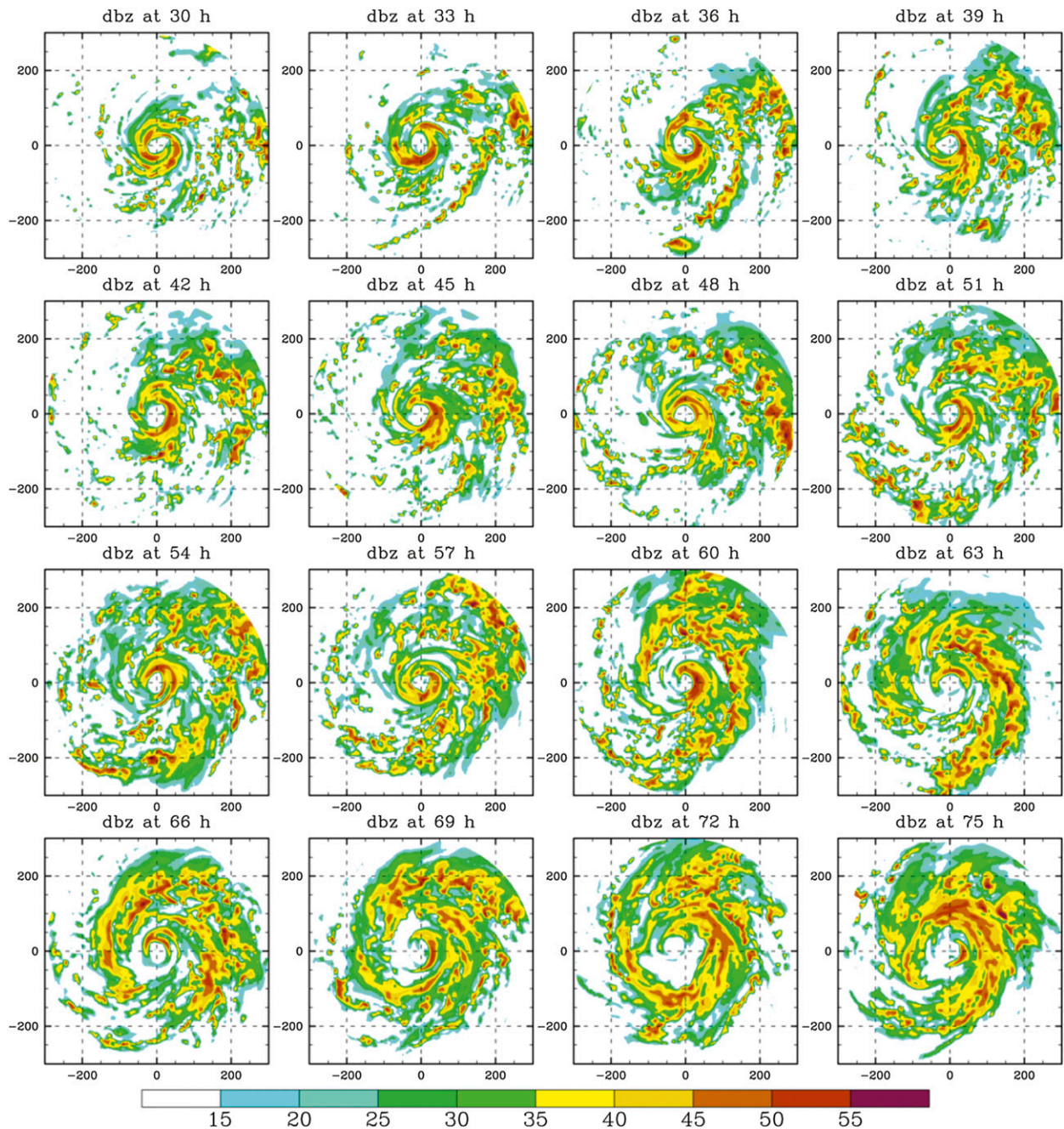


FIG. 12. Simulated radar reflectivity (dBZ) at $z = 1$ km from 30 to 75 h plotted every 3 h.

have arisen from the stratiform process induced by the ice particles in the strong outflow. The stratiform process also exists in our simulation, as evidenced by the vertical velocity maxima in the middle–upper level at the beginning. However, this phenomenon could also be partly explained by the larger vertical velocity values in the upper level in the strong convective cells. Given the collocation of the PV and the radar reflectivity maxima, we hypothesize that the main midlevel PV anomalies

come primarily from peripheral convection. To confirm our hypothesis, we performed a sensitive experiment using the Kessler warm-rain (no ice) microphysics scheme (Kessler 1969) instead of the WSM6 scheme used in the control simulation. It turns out that the SEF is also found at a similar time and location in the sensitive experiment. Therefore, the ice process may not be critical in the case of Sinlaku (2008), though it is in the other case (Zhou and Wang 2011; Fang and Zhang 2012).

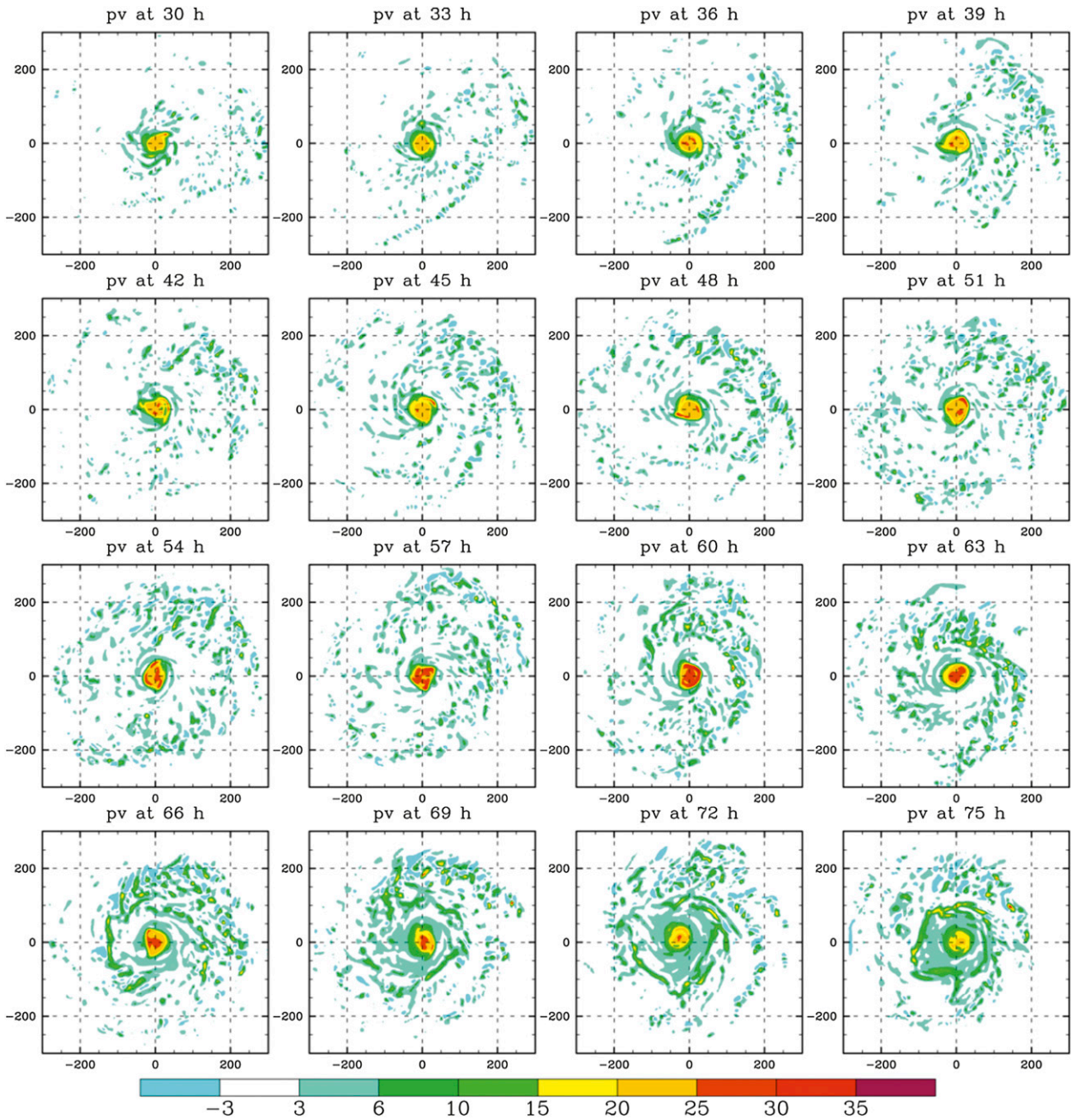


FIG. 13. As in Fig. 12, but for potential vorticity (PVU) at $z = 3$ km.

b. Vortex Rossby waves activity

As stated in the introduction, Montgomery and Kallenbach (1997) proposed that VRWs may play a role in the SEF in severe storms—a proposition supported by Qiu et al.’s (2010) idealized model simulations. However, other studies—those based on real cases—do not confirm the contribution of VRWs to the SEF (e.g., Judt and Chen 2010; Tervey et al. 2013; Judt and Chen 2013).

To clarify the issue, we now consider the potential contributions of VRWs in our simulated SEF of Sinlaku. Figure 14 shows the simulated wave-2 components of the vertical velocity (similar results are obtained for wave-3 components; not shown). As can be seen, the main wave activity is limited to the region near the primary eyewall for the whole simulation, and no sign of outward propagation in the region between the primary eyewall and the secondary eyewall is observed. The

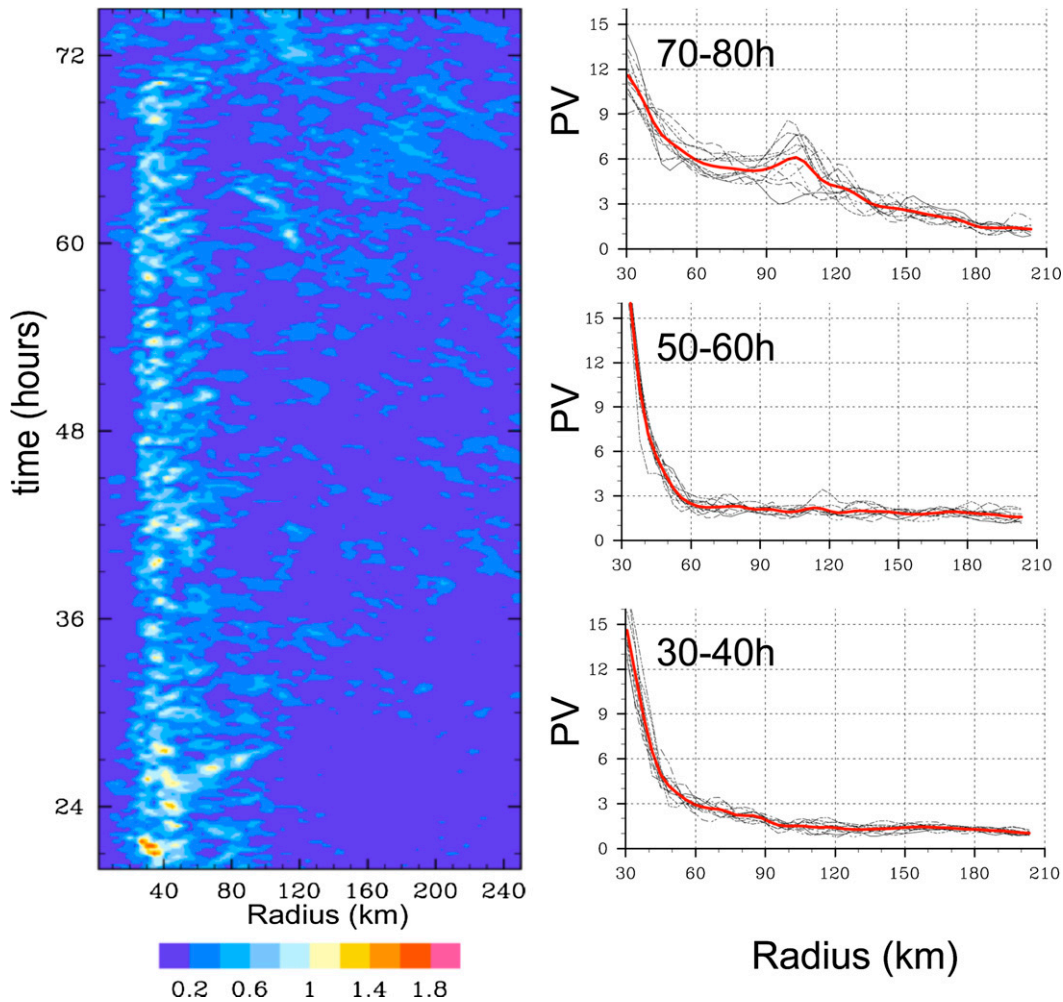


FIG. 14. (left) Time evolution of wavenumber-2 component of the vertical velocity (m s^{-1}) at 3 km from 20 to 75 h. (right) Radial PV profiles at (bottom) 30–40, (middle) 50–60, (top) 70–80 h. Red line is the time-averaged results.

radial PV profiles also give a similar scenario (Fig. 14, right panels). During the 50–60-h period, the radial PV gradients are very flat and thus do not favor the propagation of VRWs. The beta skirt, which is needed for the upward cascade referred to in Terwey and Montgomery (2008), does not appear to have any effect in our simulation.

To further understand the impact of VRWs and eddy fluxes on the structure of the simulated Sinlaku, the tangential wind tendency equation in cylindrical coordinates is calculated. The equation (Fudeyasu and Wang 2011) can be written as follows:

$$\frac{\partial \bar{v}}{\partial t} = -\bar{u}\bar{\eta} - \overline{u'\eta'} - \bar{w}\frac{\partial \bar{v}}{\partial z} - \overline{w'\frac{\partial v'}{\partial z}} + \bar{F}_\lambda. \quad (4)$$

Here η is the absolute vorticity. This equation is basically the same as Eq. (3), except that the perturbation

terms are also considered here. The five terms on the right-hand side are radial advection of the azimuthal-mean absolute angular momentum by the azimuthal-mean radial wind, radial advection by eddy processes, vertical advection of the azimuthal-mean tangential wind by the azimuthal-mean vertical velocity, vertical advection by eddy processes, and surface friction and subgrid-scale vertical mixing. Figure 15 shows the contribution of each term to the spinup process of the outer-core circulation. The result is averaged from 58 to 62 h in order to remove transient noises. The region where the SEF occurred is indicated by the red solid box. The tangential wind in the outer core has a positive tendency throughout the whole box, which is consistent with the spinup process during the SEF. The negative tendency appears in the inner eyewall and the upper troposphere. As we can see from Fig. 15, the spinup process in the boundary layer is mainly due to the mean radial advection term, whereas

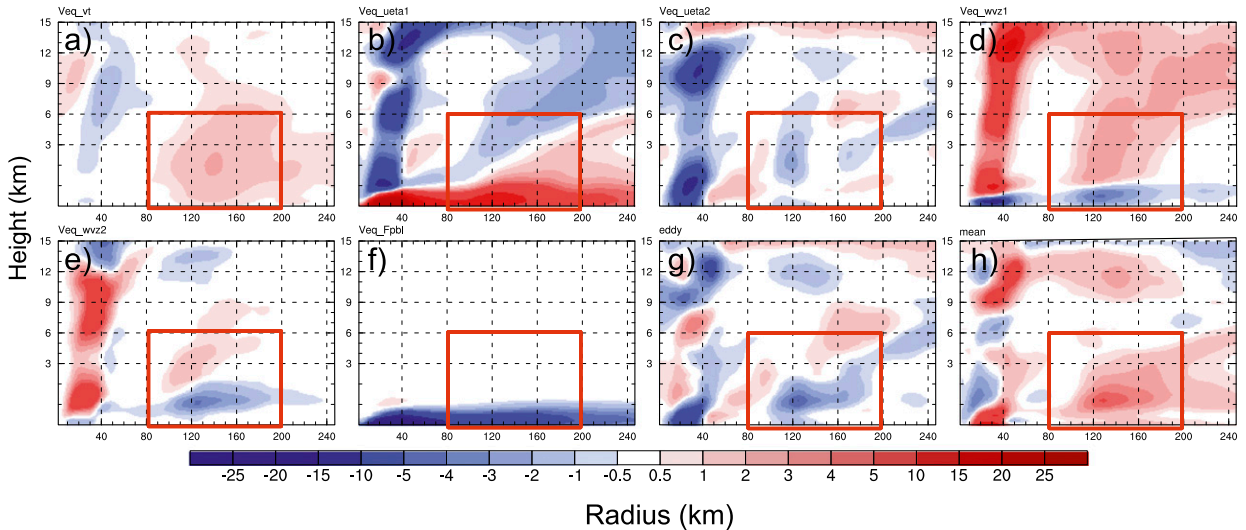


FIG. 15. (a) The tangential wind tendency ($\text{m s}^{-1} \text{h}^{-1}$) averaged from 58 to 62 h. Contribution of (b) radial advection by the azimuthal-mean radial wind ($-\bar{u}\bar{\eta}$), (c) radial advection by eddy processes ($-\bar{u}'\bar{\eta}'$), and (d) vertical advection by the azimuthal-mean vertical velocity ($-\bar{w}\partial\bar{v}/\partial z$). (e) Vertical advection by eddy processes ($-\bar{w}'\partial v'/\partial z$) and (f) surface friction forcing (\bar{F}_λ). (g) Total eddy effect [sum of (c) and (e)]. (h) Mean flow effect [sum of (b) and (d)].

the positive tendency above the boundary mainly results from vertical advection by the azimuthal-mean vertical velocity. The contribution of the second term on the rhs of the equation is almost cancelled by the fourth term (Fig. 15g). Diagnoses at earlier times (around 50 h) were also conducted, with similar results. Thus, it is evident that the eddy process including VRWs makes a relatively small contribution to the SEF in our simulation.

6. Concluding remarks

In this study, we successfully reconstructed the ERC and SEF in Typhoon Sinlaku (2008) with high temporal and spatial outputs from a high-resolution WRF simulation. Based on the WRF simulation and our experiments with the Sawyer–Eliassen equation, we established that the following physical processes lead to the SEF and ERC.

First, accompanying the intensification process of the primary eyewall, active peripheral convection (outer rainbands) develops because of the favorable environment. The convective cells that make up the outer rainbands begin to organize and move inward under strong inflow and balanced overturning circulation, as derived using the Sawyer–Eliassen equation. Second, the transverse circulation induced by the diabatic heating contributes to the expansion of the wind field (the inertial stability), which facilitates more efficient conversion of diabatic heat to kinetic energy and leads to the progressive growth of the supergradient wind. Third, this supergradient wind forces convergence and thus further enhances the convection and diabatic heating. It is this

persistent, positive feedback between the balanced response from the convective heating and the unbalanced dynamical process above and within the boundary layer that enhances the tangential wind field and convection and, thus, ultimately leads to the establishment of the secondary eyewall in the favorable SEF region. After the secondary eyewall has become established, the abrupt development of strong convection leads, in turn, to a further rapid drop in pressure and an acceleration of the inflow above and within the boundary layer in the outer region and a deceleration of the inflow in the region between the primary eyewall and the secondary eyewall. Because of the absence of a moisture supply from the inflow, the primary eyewall eventually disappears and thus the ERC is complete.

One unique aspect of the current study is to demonstrate through the S–E equation that the contribution of diabatic heating from the outer rainbands outweighs that from the primary eyewall to the secondary eyewall formation. Moreover, other than Qiu et al. (2010), it is found that there is no clear link between outer rainbands and the VRWs in our simulation, which means the environment, even far from the TC center, can be important for SEF. Our study also complements recent studies of Rozoff et al. (2012), Huang et al. (2012), Qiu and Tan (2013), and Wang et al. (2013) in understanding the interplay and positive feedback between balanced and unbalanced dynamic processes in SEF. It is believed 1) that the development of the outer rainbands and the unbalanced boundary layer processes characterized by supergradient winds and convergence should be taken

as a precursor of SEF and as a basis for predicting the SEF and 2) that the development of the outer rainbands and the coupled boundary layer processes should be taken into full consideration. At present, however, we have yet to distinguish between the relative importance of the diabatic heating, of the outer rainbands, and of the unbalanced boundary layer processes to SEF and ERC. To achieve clarification on this point, further research—including high-resolution and full-physics numerical modeling—is needed.

Acknowledgments. The authors benefited greatly from discussions with Juan Fang, who also provided the codes for solving the Sawyer–Eliassen equation. Comments provided by Christopher M. Rozoff, Chun-Chieh Wu, and another anonymous reviewer are also greatly appreciated. This research was supported by the National Basic Research Project for Typhoon (Grant 2009CB421504), the Chinese NSF (Grant 40921160380), and the U.S. NSF (Grants 063064 and 0840651).

APPENDIX

Sawyer–Eliassen Equation

In this paper, the following Sawyer–Eliassen equation in pseudoheight coordinates is used (Eliassen 1951; Montgomery et al. 2006; Fudeyasu and Wang 2011; Fang and Zhang 2011):

$$\begin{aligned} \frac{\partial}{\partial r} \left(\frac{A}{r} \frac{\partial \bar{\psi}}{\partial r} + \frac{B}{r} \frac{\partial \bar{\psi}}{\partial z} \right) + \frac{\partial}{\partial z} \left(\frac{C}{r} \frac{\partial \bar{\psi}}{\partial z} + \frac{B}{r} \frac{\partial \bar{\psi}}{\partial r} \right) \\ = -\frac{\partial(\bar{\xi}F)}{\partial z} + \frac{\partial \bar{Q}}{\partial r}, \end{aligned} \quad (\text{A1})$$

where $\bar{\psi}$ is the mean transverse streamfunction, which is related to the mean radial velocity \bar{u} and the vertical velocity \bar{w} by $\bar{u} = -(1/r)\partial\bar{\psi}/\partial z$, $\bar{w} = (1/r)\partial\bar{\psi}/\partial r$. The parameters $A = \bar{N}^2 = (g/\theta_0)\partial\bar{\theta}/\partial z$, $B = -\bar{\xi}\partial\bar{v}/\partial z$, $C = \bar{\xi}\bar{\eta}$, and $z = (C_p\theta_0/g)[1 - (p/p_0)^{R/C_p}]$, where \bar{v} is the azimuthal-mean tangential velocity; $\bar{\eta}$ is the azimuthal-mean absolute vertical vorticity; and C is the vortex inertial parameter. The terms F and Q on the right-hand side of Eq. (A1) are defined, respectively, as

$$\begin{aligned} F &= -\overline{u'v'} - \overline{w' \frac{\partial v'}{\partial z}} + \overline{F_\lambda}, \\ \bar{Q} &= \frac{g}{\theta_0} \left(-\overline{u' \frac{\partial \theta'}{\partial r}} - \overline{w' \frac{\partial \theta'}{\partial z}} + \bar{\theta} \right), \end{aligned} \quad (\text{A2})$$

which represent the momentum forcing and diabatic heating, respectively. The quantities with the primes

denote the deviations from the azimuthal mean, called eddies. The first two terms in F are contributions from the momentum forcing associated with the eddies, and the last term represents the contribution of the subgrid-scale processes and the friction, which can be obtained directly in WRF. The first two terms in Q represent the eddies' contribution to heating, and the last term in Q is the azimuthally mean diabatic heating rate. For the meanings of other symbols and the calculation techniques, the readers are referred to Fudeyasu and Wang (2011) for details.

REFERENCES

- Abarca, S. F., and K. L. Corbosiero, 2011: Secondary eyewall formation in WRF simulations of Hurricanes Rita and Katrina (2005). *Geophys. Res. Lett.*, **38**, L07802, doi:10.1029/2011GL047015.
- Bell, M. M., M. T. Montgomery, and W.-C. Lee, 2012: An axisymmetric view of concentric eyewall evolution in Hurricane Rita (2005). *J. Atmos. Sci.*, **69**, 2414–2432.
- Bui, H. H., R. K. Smith, M. T. Montgomery, and J. Peng, 2009: Balanced and unbalanced aspect of tropical cyclone intensification. *Quart. J. Roy. Meteor. Soc.*, **135**, 1715–1731.
- Chen, Y., and M. K. Yau, 2001: Spiral bands in a simulated hurricane. Part I: Vortex Rossby wave verification. *J. Atmos. Sci.*, **58**, 2128–2145.
- Didlake, A. C., Jr., and R. A. Houze Jr., 2011: Kinematics of the secondary eyewall observed in Hurricane Rita (2005). *J. Atmos. Sci.*, **68**, 1620–1636.
- , and —, 2013: Convective-scale variations in the inner-core rainbands of a tropical cyclone. *J. Atmos. Sci.*, **70**, 504–523.
- Dritschel, D. G., and D. W. Waugh, 1992: Quantification of the inelastic interaction of unequal vortices in two two-dimensional vortex dynamics. *Phys. Fluids*, **4A**, 1737–1774.
- Eliassen, A., 1951: Slow thermally or frictionally controlled meridional circulation in a circular vortex. *Astrophys. Norv.*, **5**, 19–60.
- Elsberry, R. L., and P. A. Harr, 2008: Tropical cyclone structure (TCS08) field experiment science basis, observational platforms, and strategy. *Asia-Pac. J. Atmos. Sci.*, **44**, 209–231.
- Emanuel, K., C. DesAutels, C. Holloway, and R. Korty, 2004: Environmental control of tropical cyclone intensity. *J. Atmos. Sci.*, **61**, 843–858.
- Enagonio, J., and M. T. Montgomery, 2001: Tropical cyclogenesis via convectively forced vortex Rossby waves in shallow water primitive equation model. *J. Atmos. Sci.*, **58**, 685–706.
- Fang, J., and F. Zhang, 2010: Initial development and genesis of Hurricane Dolly (2008). *J. Atmos. Sci.*, **67**, 655–672.
- , and —, 2011: Evolution of multiscale vortices in the development of Hurricane Dolly (2008). *J. Atmos. Sci.*, **68**, 103–122.
- , and —, 2012: Effect of beta shear on simulated tropical cyclones. *Mon. Wea. Rev.*, **140**, 3327–3346.
- Fudeyasu, H., and Y. Wang, 2011: Balanced contribution to the intensification of a tropical cyclone simulated in TCM4: Outer-core spinup process. *J. Atmos. Sci.*, **68**, 430–449.
- Hawkins, J. D., M. Helveston, T. F. Lee, F. J. Turk, K. Richardson, C. Sampson, J. Kent, and R. Wade, 2006: Tropical cyclone multiple eyewall characteristics. Preprints, *27th Conf. on Hurricane and Tropical Meteorology*, Monterey, CA, Amer. Meteor. Soc., 6B.1. [Available online at http://ams.confex.com/ams/27Hurricanes/techprogram/paper_108864.htm.]
- Hill, K. A., and G. M. Lackmann, 2009: Influence of environmental humidity on tropical cyclone size. *Mon. Wea. Rev.*, **137**, 3294–3315.

- Hong, S.-Y., J. Dudhia, and S.-H. Chen, 2004: A revised approach to ice microphysical processes for the parameterization of clouds and precipitation. *Mon. Wea. Rev.*, **132**, 103–120.
- , Y. Noh, and J. Dudhia, 2006: A new vertical diffusion package with an explicit treatment of entrainment processes. *Mon. Wea. Rev.*, **134**, 2318–2341.
- Houze, R. A., Jr., S. S. Chen, B. F. Smull, W.-C. Lee, and M. M. Bell, 2007: Hurricane intensity and eyewall replacement. *Science*, **315**, 1235–1239.
- Huang, Y.-H., M. T. Montgomery, and C.-C. Wu, 2012: Concentric eyewall formation in Typhoon Sinlaku (2008). Part II: Axisymmetric dynamical processes. *J. Atmos. Sci.*, **69**, 662–674.
- Judt, F., and S. S. Chen, 2010: Convectively generated vorticity in rainbands and formation of the secondary eyewall in Hurricane Rita of 2005. *J. Atmos. Sci.*, **67**, 3581–3599.
- , and —, 2013: Reply to “Comments on ‘Convectively generated potential vorticity in rainbands and formation of the secondary eyewall in Hurricane Rita of 2005.’” *J. Atmos. Sci.*, **70**, 989–992.
- Kessler, E., 1969: *On the Distribution and Continuity of Water Substance in Atmospheric Circulation*. Meteor. Monogr., No. 32, Amer. Meteor. Soc., 84 pp.
- Kuo, H.-C., L.-Y. Lin, C.-P. Chang, and R. T. Williams, 2004: The formation of concentric vorticity structures in typhoons. *J. Atmos. Sci.*, **61**, 2722–2734.
- , W. H. Schubert, C.-L. Tsai, and Y.-F. Kuo, 2008: Vortex interactions and barotropic aspects of concentric eyewall formation. *Mon. Wea. Rev.*, **136**, 5183–5198.
- , C.-P. Chang, Y.-T. Yang, and H.-J. Jiang, 2009: Western North Pacific typhoons with concentric eyewalls. *Mon. Wea. Rev.*, **137**, 3758–3770.
- Martinez, Y., G. Brunet, M. K. Yau, and X. Wang, 2011: On the dynamics of concentric eyewall genesis: Space–time empirical normal modes diagnosis. *J. Atmos. Sci.*, **68**, 457–476.
- Menelaou, K., M. K. Yau, and Y. Martinez, 2012: On the dynamics of the secondary eyewall genesis in Hurricane Wilma (2005). *Geophys. Res. Lett.*, **39**, L04801, doi:10.1029/2011GL050699.
- Meng, Z., and F. Zhang, 2008a: Tests of an ensemble Kalman filter for mesoscale and regional-scale data assimilation. Part III: Comparison with 3DVAR in a real-data case study. *Mon. Wea. Rev.*, **136**, 522–540.
- , and —, 2008b: Tests of an ensemble Kalman filter for mesoscale and regional-scale data assimilation. Part IV: Comparison with 3DVAR in a month-long experiment. *Mon. Wea. Rev.*, **136**, 3671–3682.
- Montgomery, M. T., and R. J. Kallenbach, 1997: A theory for vortex Rossby-waves and its application to spiral bands and intensity changes in hurricanes. *Quart. J. Roy. Meteor. Soc.*, **123**, 435–465.
- , M. E. Nicholls, T. A. Cram, and A. B. Saunders, 2006: A vertical hot tower route to tropical cyclogenesis. *J. Atmos. Sci.*, **63**, 355–386.
- Moon, Y., and D. S. Nolan, 2010: The dynamic response of the hurricane wind field to spiral rainband heating. *J. Atmos. Sci.*, **67**, 1779–1805.
- , —, and M. Iskandarani, 2010: On the use of two-dimensional flow to study secondary eyewall formation in tropical cyclones. *J. Atmos. Sci.*, **67**, 3765–3773.
- Qiu, X., and Z.-M. Tan, 2013: The roles of asymmetric inflow forcing induced by outer rainbands in tropical cyclone secondary eyewall formation. *J. Atmos. Sci.*, **70**, 953–974.
- , —, and Q. Xiao, 2010: The role of vortex Rossby waves in hurricane secondary eyewall formation. *Mon. Wea. Rev.*, **138**, 2092–2109.
- Rozoff, C. M., W. H. Schubert, B. D. McNoldy, and J. P. Kossin, 2006: Rapid filamentation zones in intense tropical cyclones. *J. Atmos. Sci.*, **63**, 325–340.
- , D. S. Nolan, J. P. Kossin, F. Zhang, and J. Fang, 2012: The roles of an expanding wind field and inertial stability in tropical cyclone secondary eyewall formation. *J. Atmos. Sci.*, **69**, 2621–2643.
- Shapiro, L. J., and H. E. Willoughby, 1982: The response of balanced hurricanes to local sources of heat and momentum. *J. Atmos. Sci.*, **39**, 378–394.
- Sitkowski, M., J. Kossin, and C. M. Rozoff, 2011: Intensity and structure changes during hurricane eyewall replacement cycles. *Mon. Wea. Rev.*, **139**, 3829–3847.
- Skamarock, W. C., and Coauthors, 2008: A description of the Advanced Research WRF version 3. NCAR Tech. Note NCAR/TN-475+STR, 113 pp. [Available online at http://www.mmm.ucar.edu/wrf/users/docs/arw_v3.pdf.]
- Smith, R. K., M. T. Montgomery, and N. V. Sang, 2009: Tropical cyclone spin-up revisited. *Quart. J. Roy. Meteor. Soc.*, **135**, 1321–1335.
- Terwey, W. D., and M. T. Montgomery, 2008: Secondary eyewall formation in two idealized, full-physics modeled hurricanes. *J. Geophys. Res.*, **113**, D12112, doi:10.1029/2007JD008897.
- , S. F. Abarca, and M. T. Montgomery, 2013: Comments on “Convectively generated potential vorticity in rainbands and formation of the secondary eyewall in Hurricane Rita of 2005.” *J. Atmos. Sci.*, **70**, 984–988.
- Wang, X., Y.-M. Ma, and N. E. Davidson, 2013: Secondary eyewall formation and eyewall replacement cycles in a simulated hurricane: Effect of the net radial force in the hurricane boundary layer. *J. Atmos. Sci.*, **70**, 1317–1341.
- Wang, Y., 2002a: Vortex Rossby waves in a numerically simulated tropical cyclone. Part I: Overall structure, potential vorticity, and kinetic energy budgets. *J. Atmos. Sci.*, **59**, 1213–1238.
- , 2002b: Vortex Rossby waves in a numerically simulated tropical cyclone. Part II: The role in tropic cyclone structure and intensity changes. *J. Atmos. Sci.*, **59**, 1239–1262.
- , 2009: How do outer spiral rainbands affect tropical cyclone structure and intensity? *J. Atmos. Sci.*, **66**, 1250–1273.
- , and C.-C. Wu, 2004: Current understanding of tropical cyclone structure and intensity changes—A review. *Meteor. Atmos. Phys.*, **87**, 257–278.
- Willoughby, H. E., J. A. Clos, and M. G. Shoreibah, 1982: Concentric eye walls, secondary wind maxima, and the evolution of the hurricane vortex. *J. Atmos. Sci.*, **39**, 395–411.
- Wu, C.-C., H.-J. Cheng, Y. Wang, and K.-H. Chou, 2009: A numerical investigation of the eyewall evolution of a landfalling typhoon. *Mon. Wea. Rev.*, **137**, 21–40.
- , G.-Y. Lien, J.-H. Chen, and F. Zhang, 2010: Assimilation of tropical cyclone track and structure based on the ensemble Kalman filter (EnKF). *J. Atmos. Sci.*, **67**, 3806–3822.
- , Y.-H. Huang, and G.-Y. Lien, 2012: Concentric eyewall formation in Typhoon Sinlaku (2008). Part I: Assimilation of T-PARC data based on the ensemble Kalman filter (EnKF). *Mon. Wea. Rev.*, **140**, 506–527.
- Xu, J., and Y. Wang, 2010a: Sensitivity of tropical cyclone inner core size and intensity to the radial distribution of surface entropy flux. *J. Atmos. Sci.*, **67**, 1831–1852.
- , and —, 2010b: Sensitivity of the simulated tropical cyclone inner-core size to the initial vortex size. *Mon. Wea. Rev.*, **138**, 4135–4157.
- Zhou, X., and B. Wang, 2011: Mechanism of concentric eyewall replacement cycles and associated intensity change. *J. Atmos. Sci.*, **68**, 972–988.